

Formation of deformation twin boundaries in a coarse-grained aluminum

Shenbao Jin¹, Kai Zhang¹, Ruben Bjørge², Nairong Tao³, Knut Marthinsen¹, Ke Lu³ and Yanjun Li^{1,*}

1. Department of Materials Science and Engineering, Norwegian University of Science and Technology,

7491 Trondheim, Norway

2. SINTEF Materials and Chemistry, 7465 Trondheim, Norway

3. Shenyang National Laboratory for Materials Science, Institute of Metal Research, Chinese Academy of

Sciences, Shenyang, 110016, China

*** Corresponding author at: Department of Materials Science and Engineering,**

Norwegian University of Science and Technology, 7491 Trondheim, Norway

E-mail address: Yanjun.Li@ntnu.no (Y.J. Li).

Abstract

Deformation twinning has rarely been observed in aluminum and its alloys because of their high stacking fault energy (SFE). Here, we report that a significant amount of $\Sigma 3$ deformation twins could be generated in a coarse-grained Al-7Mg alloy by dynamic plastic deformation (DPD). A systematic investigation of the $\Sigma 3$ boundaries shows that they are $\Sigma 3\{112\}$ type incoherent twin boundaries (ITBs). These ITBs have formed by gradual evolution from copious low-angle deformation bands through $\langle 111 \rangle$ -twist Σ boundaries by lattice rotation. These findings provide an approach to generate deformation twin boundaries in high SFE metallic alloys. It is suggested that high solution content of Mg in the alloy and the special deformation mode of DPD played an important role in formation of the Σ and ITBs.

In recent years, nano-twinned metals and alloys, like copper and austenite steels¹⁻⁴ have attracted great interest because of their superior combination of strength and ductility. The ultrahigh strength originates from the stable nature of the $\Sigma 3\{111\}$ coherent twin boundaries (CTBs) as they present strong barriers to dislocation glide. At the same time, the CTBs enable absorption and transmission of dislocations and hence contribute significantly to macroscopic ductility.⁵ Up to now, several methods have been developed for fabrication of nano-twinned materials, such as pulsed electrodeposition,⁶⁻⁸ magnetron sputtering,^{9,10} and dynamic plastic deformation (DPD).^{11,12} Note that the above mentioned methods are mainly for metals with low stacking fault energy (SFE) or a low ratio of unstable twinning (γ_{ut}) to unstable stacking energy (γ_{us}). In aluminum and aluminum alloys, however, because of their high SFEs and high γ_{ut}/γ_{us} ratio, twinning can only occur under some extreme conditions such as at crack tips,¹³⁻¹⁵ during severe plastic deformation of nanocrystalline materials,¹⁶⁻²¹ and during epitaxial growth of nano layered Al by using Ag as seed layer.²²⁻²⁴ In coarse grained aluminum, no deformation twins have ever been observed, though Han et al.²⁵ argued that microtwins could form in aluminum single crystals subjected to equal channel angular pressing.

In this letter we report that, instead of coherent deformation twins, a large fraction of incoherent deformation twins could be generated in a coarse-grained Al-7Mg (in wt.%) alloy during dynamic plastic deformation through a mechanism of crystal rotation of deformation bands.

The Al-7Mg alloy studied in this work was prepared by using commercial pure Al and high purity Mg. Cylindrical samples with dimension of $\text{Ø}24 \times 16\text{mm}$ were machined from a DC-cast Al-7Mg ingot and homogenized in an air circulation furnace at 500°C for 3h, followed by water quenching. The average grain size of the sample before DPD was $\sim 75\mu\text{m}$, with a random texture. After the homogenization heat treatment, the alloy becomes single phased and all the Mg content is kept in solid solution in the Al-matrix.^{26,27} During

DPD, the samples were deformed by multiple impact loading using an upper anvil in a drop tower at room temperature with a strain rate of 10^2 - 10^3 s⁻¹. During each impact, the height reduction of the sample was 2mm. The deformation strain $\epsilon = \ln(L_0/L_f)$, where L_0 and L_f are initial and final sample thickness, respectively. The largest strain achieved in the DPD-ed samples is 1.73 (with ten impacts). After DPD, electron backscattered diffraction (EBSD) analysis was conducted on longitudinal sections (parallel to the cylinder axis) of the samples with the largest and also some intermediate strains. Detailed information about DPD and EBSD can be found in Ref. [28].

Fig. 1(a) shows a typical grain boundary (GB) structure of the DPD sample subjected to an accumulated deformation strain of 1.31. The deformed structure is composed of elongated coarse grains and fine equiaxed grains. It is interesting to see that a large fraction (>6%) of the grain boundaries between the elongated grains were identified as 60° coincidence site lattice (CSL) $\Sigma 3$ GBs by the EBSD-TSL software. This fraction is much larger than the fraction of random $\Sigma 3$ boundaries. To further investigate the $\Sigma 3$ grain boundaries, the $\{111\}$ and $\{101\}$ poles of Grain 1 and 2 labeled in Fig. 1(a) were drawn in the same pole figures in Fig. 1(b), respectively. As can be seen, they share one $\{111\}$ pole and three sets of $\{101\}$ poles, which means that these two grains have a twin orientation relationship. The $\{111\}$ traces of grains 1 and 2 at the sample surface are also indicated by arrows in Fig. 1(a). It shows, however, that the GB between the two grains is not parallel to any of the $\{111\}$ traces, which indicates that it is not a coherent $\{111\}$ twin boundary. A comparison of the GB trace with surface traces of different possible planes shows that the $\Sigma 3$ GB is closely parallel to (121) and (21 $\bar{1}$) in Grain 1 and 2, respectively, implying that the GB plane is likely on the $\{112\}$ planes. A similar single-surface trace analysis was done on totally fifty-six $\Sigma 3$ GBs and it is found that most (50 of 56) of the $\Sigma 3$ GBs are close to $\{112\}$ traces. The indices of all the measured GB traces were determined and their poles

are drawn in the (001) stereographic projection shown in Fig. 1(c). As each GB trace vector may have two different indexes according to two neighboring grains, totally 112 pole points were included. As indicated, all the poles are located close to the large circle of $\{112\}$ planes, implying that the $\Sigma 3$ GBs are on the $\{112\}$ planes and most of the boundaries are of $\Sigma 3\{112\}$ ITBs.

The supposed $\{112\}$ type grain boundary planes of the $\Sigma 3$ GBs in DPD sample have been confirmed by a serial sectioning EBSD study [29] of selected GBs, by which the inclination angle of the grain boundary planes to sample surface can be determined. Fig. 2(a) shows an example of such studies. The distance between the two scanning surfaces (Layers 1 and 2), Δd is about $19.0\mu\text{m}$ while the displacement of the $\Sigma 3$ boundary (GB1) in these two layers, Δs , is $3.7\mu\text{m}$ in average. Hence, the inclination angle θ of the boundary plane of GB1 to the sample surface is calculated as 79.0° , which is very close to the inclination angle of (121) with the sample surface plane $(-2-35)$, 78.5° , confirming that the boundary plane of GB1 is on $\{112\}$.

With the aim to reveal how the incoherent deformation twins formed in the alloy, the deformation structure of the samples subjected to lower accumulated deformation strains have been studied by EBSD. At low strains, there is less $\Sigma 3\{112\}$ ITBs, but a large fraction of CSL boundaries with higher Σ values, including $\Sigma 7$ $38.2^\circ \langle 111 \rangle$, $\Sigma 13b$ $27.8^\circ \langle 111 \rangle$, $\Sigma 21a$ $21.8^\circ \langle 111 \rangle$, $\Sigma 31a$ $17.9^\circ \langle 111 \rangle$ and $\Sigma 43a$ $15.2^\circ \langle 111 \rangle$. Interestingly, all of these CSL boundaries have a common feature: a $\langle 111 \rangle$ rotation axis. Fig. 3 shows the evolution of the fractions of different CSL boundaries as a function of deformation strain. As can be seen, the fraction of the high Σ value CSL boundaries decreases while the fraction of low value Σ value CSL boundaries increases with increasing deformation strain. It implies that the ITBs could gradually evolve from the higher Σ value CSL boundaries during DPD. This has been confirmed by a closer examination of the CSL boundaries. Frequently, segments of CSL boundaries with different Σ values can be found co-existing in the

same GB. As shown in the upper right corner of Fig. 4(a), the long GB in the center of the grain is composed of segments of different misorientation angles from 12.5 to 27.6°. More interestingly, the $\Sigma 13b$ and $\Sigma 21a$ boundary segments are alternating in the same boundaries, implying the grain boundary is in the process of transforming from low angle grain boundaries (LAGB) to $\Sigma 21a$ and from $\Sigma 21a$ to $\Sigma 13b$. Fig. 4(b) shows another example for the transformation from $\Sigma 7$ 38.2° $\langle 111 \rangle$ boundary to $\Sigma 3\{112\}$ boundary through the intermediate stage of 47.4° misorientation GB.

The copious deformation bands (DBs), similar to those shown in the lower left corner of Fig. 4(a), can be observed frequently in some grains. In the figure, parallel DBs with LAGBs of different misorientation angles in range of 5-15° (Fig. 4c) can be seen. The point-to-origin misorientation curve shows that a considerable misorientation gradient exists in the DBs, which is more evident in the relatively wider ones, implying that these DBs form by lattice rotation. As indicated by the arrows in Fig. 4(a), the DBs are parallel to the traces of $\{111\}$ planes. The poles of the boundary traces of the copious DBs in the sample deformed to $\epsilon=0.27$ were drawn in the $[001]$ stereographic projection, Fig. 4(d). As can be seen, all the poles are located on the $\{111\}$ large circles (within 5° deviation), showing that all the DBs have $\{111\}$ planes as boundary plane. However, after deformed to higher deformation strains, such DBs can rarely be observed, suggesting that most of them have transformed into $\langle 111 \rangle$ CSL twist GBs or $\Sigma 3\{112\}$ boundaries.

The formation of the copious DBs in the alloy should be attributed to the special deformation character of Al-Mg alloys with a high content of Mg, which, unlike most other Al alloys, deforms mainly by planar glide.²⁸ The tendency for planar glide increases with increasing Mg content and strain rate.^{30,31} As a result of planar glide, $\{111\}$ twist boundaries composed of dislocations walls on $\{111\}$ form.³¹⁻³⁴ In this work, it is found that copious DBs mostly form in those grains that have only one preferential slip system (the Schmidt

factor is much larger than other slip systems). It is in agreement with the hypothesis that the formation of copious DBs is closely related to the deformation by one or two slip systems.³⁵ During DPD process, the mono-directional impact loading makes it possible for the planar glide to continue until the misorientation of the $\{111\}$ twist boundaries increase to a relatively high misorientation angle. Since the CSL boundaries have lower interfacial energy than the random GBs, the CSL boundaries with $\Sigma=21a$ (21.8°), $13b$ (27.8°) and 7 (35.2°) are more frequently observed. However, it has to be noted that the CSL grain boundary planes gradually change away from $\{111\}$ planes with increasing the misorientation angle and the decreasing of the Σ value. Actually, for the $38.2^\circ \Sigma 7$ boundaries, the boundary planes on both sides of GBs have already rotated far away from $\{111\}$. The reason why the GB planes, instead of keeping on the same $\{111\}$ plane, evolve from $\{111\}$ to $\{112\}$, may be due to the lattice rotation of the sub grains during deformation with the trend to have one of their $\langle 110 \rangle$ directions parallel to loading direction (as shown by the red arrow (bottom right) in Fig. 1b). Once one of $\langle 110 \rangle$ directions is rotated to be close to the loading direction, new dislocation slip systems on different $\{111\}$ planes will be activated, causing the tilting of the grain boundary plane away from the original $\{111\}$ twist plane of the DBs. Considering that the $\{112\}$ planes are low-index planes and have a relatively small angle to $\{111\}$, 19.5° , it is not surprising that $\Sigma 3\{112\}$ twist boundaries could form. The formation of copious deformation bands, CSL $\{111\}$ twist boundaries and $\Sigma 3\{112\}$ twins should also be attributed to the high strain rate nature of DPD, which makes the deformation in each single impact loading can last to a higher deformation strain via the same slip system before another more favorite slip system is activated. However, how the GB planes of DBs change from $\{111\}$ planes to $\{112\}$ planes of $\Sigma 3$ type needs more thorough experimental and simulation studies.

It has been reported that the coherent $\Sigma 3\{111\}$ twins can form in pure nano-crystalline Al (50-100nm) at

RT under high strain rate conditions ($5 \times 10^5 \text{ s}^{-1}$).^{19,20} However, since the strain rate during DPD is much lower ($10^2\text{-}10^3 \text{ s}^{-1}$) and the grain size in the DPD-ed samples generally in micron scale (even in the sample subjected to the largest deformation strain), it is not surprising that no $\{111\}$ coherent twinning formed in these DPD Al-7Mg samples even with a reduced SFE by high Mg contents. Compared to coherent $\Sigma 3\{111\}$ twin boundaries, $\Sigma 3\{112\}$ incoherent twin boundaries (ITBs) have been less studied.^{36,37} It has been found that the $\Sigma 3\{112\}$ ITBs have a larger mobility than coherent twin boundaries. According to Li et al.,³⁸ slip bands can transmit through ITBs in Cu, and the penetrability and mobility of the ITBs contribute to a higher fatigue cracking resistance. Bufford et al.³⁹ suggested that the ITBs in Al can effectively resist the pile-up of dislocations and lead to significant work hardening. Through measuring internal friction on Al bicrystals with various $\langle 111 \rangle$ tilt and twist grain boundaries (GBs), Jiang et al.⁴⁰ suggested that both CTBs and ITBs possess a high resistance to atomic rearrangement and thus have a high structural stability.

A high fraction of low Σ value CSL boundaries in polycrystals can be beneficial for an improvement of the mechanical properties, such as intergranular-cracking, -corrosion, and -creep, which is the basic hypothesis for “grain boundary engineering (GBE)”.^{41,42} Unfortunately, the idea of GBE can in generally not be achieved in aluminum and its alloys, because of their wavy-slip deformation mode and high SFEs, which makes the formation of twin and CSL boundaries difficult. Strikingly, the results in the present paper indicate that GBE can still be possible for high SFE materials. Since the formation of ITBs and CSL boundaries in Al-7Mg alloy was closely correlated with the copious DBs which only formed in those grains with single dislocation slip systems, a significant increase of the fraction of CSL boundaries and $\Sigma 3\{112\}$ ITBs can be expected by a well-designed texture and crystal orientation of the original material in relation to the loading direction of DPD.

In summary, a substantial fraction of $\Sigma 3\{112\}$ ITBs was generated in a coarse-grained Al alloy by DPD. It is revealed that the ITBs evolve from copious low-angle $\langle 111 \rangle$ -twist DBs through CSL boundaries. Such a deformation mechanism is attributed to the special planar glide deformation mode of the Al-7Mg alloy and the special loading mode of DPD in terms of high strain rate and mono-directional impact loading. These findings shed light on the deformation mechanism of planar glide type alloys during DPD and provide a potential route to generate incoherent deformation twins in high SFE metallic materials.

Acknowledgements

Financial support from Research Council of Norway, under the FRINATEK project 'BENTMAT' (Project number 222173) is gratefully acknowledged.

References

- ¹L. Lu, X. Chen, X. Huang, and K. Lu, *Science* **323**(5914), 607 (2009).
- ²K. Lu, L. Lu, and S. Suresh, *Science* **324**(5925), 349 (2009).
- ³X. Y. Li, Y. J. Wei, L. Lu, K. Lu, and H. J. Gao, *Nature* **464**(7290), 877 (2010).
- ⁴B. Gludovatz, A. Hohenwarther, D. Catoor, E. H. Chang, E. P. George, and R. O. Ritchie, *Science* **345**(6201), 1153 (2014).
- ⁵L. Lu, M. L. Sui, and K. Lu, *Science* **287**(5457), 1463 (2000).
- ⁶E. Ma, Y. M. Wang, Q. H. Lu, M. L. Sui, L. Lu and K. Lu, *Appl. Phys. Lett.* **85**(21), 4932 (2004).
- ⁷L. Lu, Y. F. Shen, X. H. Chen, L. H. Qian, and K. Lu, *Science* **304**(5669), 422 (2004).
- ⁸D. Xu, W. L. Kwan, K. Chen, X. Zhang, V. Ozoliņš, and K. N. Tu, *Appl. Phys. Lett.* **91**(25), 254105 (2007).
- ⁹X. Zhang, A. Misra, H. Wang, M. Nastasi, J. D. Embury, T. E. Mitchell, R. G. Hoagland and J. P. Hirth, *Appl. Phys. Lett.* **84**(7), 1096 (2004).

- ¹⁰O. Anderoglu, A. Misra, H. Wang, F. Ronning, M. F. Hundley, and X. Zhang, *Appl. Phys. Lett.* **93**(8), 083108 (2008).
- ¹¹Y. Zhang, Y. S. Li, N. R. Tao, and K. Lu, *Appl. Phys. Lett.* **91**(21), 211901 (2007).
- ¹²Y. S. Li, N. R. Tao, and K. Lu, *Acta Mater.* **56**(2), 230 (2008).
- ¹³R. C. Pond and L. M. F. Garcia-Garcia, *Inst. Phys. Conf. Ser.* **61**, 495 (1981).
- ¹⁴S. Hai and E. B. Tadmor, *Acta Mater.* **51**(1), 117 (2003).
- ¹⁵B. Q. Li, M. L. Sui, B. Li, E. Ma, and S. X. Mao, *Phys. Rev. Lett.* **102**(20), 205504 (2009).
- ¹⁶M. W. Chen, E. Ma, K. J. Hemker, H. W. Sheng, Y. M. Wang, and X. M. Cheng, *Science* **300**(5623), 1275 (2003).
- ¹⁷X. Z. Liao, F. Zhou, E. J. Lavernia, D. W. He, and Y. T. Zhu, *Appl. Phys. Lett.* **83**(24), 5062 (2003).
- ¹⁸Y. T. Zhu, X. Z. Liao, S. G. Srinivasan, Y. H. Zhao, M. I. Baskes, F. Zhou, and E. J. Lavernia, *Appl. Phys. Lett.* **85**(21), 5049 (2004).
- ¹⁹B. Li, B. Cao, K. Ramesh, and E. Ma, *Acta Mater.*, 57(15), 4500 (2009).
- ²⁰B. Cao, N. P. Daphalapurkar, and K. T. Ramesh, *Meccanica*, 50, 561 (2015).
- ²¹N. P. Daphalapurkar and K. T. Ramesh, *J. Mech. Phys. Solids.* 60, 277 (2012).
- ²²D. Bufford, Y. Liu, Y. Zhu, Z. Bi, Q. X. Jia, H. Wang, and X. Zhang, *Mater. Res. Lett.* **1**(1), 51 (2013).
- ²³D. Bufford, Z. Bi, Q. X. Jia, H. Wang, and X. Zhang, *Appl. Phys. Lett.* **101**(22), 223112 (2012).
- ²⁴K. Y. Yu, D. Bufford, Y. Chen, Y. Liu, H. Wang, and X. Zhang, *Appl. Phys. Lett.* **103**(18), 181903 (2013).
- ²⁵W. Z. Han, G. M. Cheng, S. X. Li, S. D. Wu, and Z. F. Zhang, *Phys. Rev. Lett.* **101**(11), 115505 (2008).
- ²⁶M. Zha, Y. J. Li, R. H. Mathiesen, R. Bjørge, and H. J. Roven, *Mater. Sci. Eng. A* **586**, 374 (2013).
- ²⁷M. Zha, Y. J. Li, R. H. Mathiesen, R. Bjørge, and H. J. Roven, *Acta Mater.* **84**, 42 (2015).

- ²⁸S. B. Jin, N. R. Tao, K. Marthinsen, and Y. J. Li, *Mater. Sci. Eng. A* **628**, 160 (2015).
- ²⁹H. Sharma, S. M. C. Van Bohemen, R. H. Petrov, and J. Sietsma, *Acta Mater.* **58**(7), 2399 (2010).
- ³⁰D. A. Hughes, *Acta Metall. Mater.* **41**(5), 1421 (1993).
- ³¹F. R. N. Nabarro and M. S. Duesbery, *Dislocations in Solids*, Vol. 11 (Elsevier, Amsterdam, 2002).
- ³²J. C. Huang and G. T. Gray III, *Acta Metall.* **37**(12), 3335 (1989).
- ³³D. Caillard and J. L. Martin, *Acta Metall.* **30**(2), 437 (1982).
- ³⁴L. E. Murr and E. V. Esquivel, *J. Mater. Sci.* **39**(4), 1153 (2004).
- ³⁵D. Kuhlmann-Wilsdorf, *Acta Mater.* **47**(6), 1697 (1999).
- ³⁶J. Wang, O. Anderoglu, J. P. Hirth, A. Misra, and X. Zhang, *Appl. Phys. Lett.* **95**(2), 021908 (2009).
- ³⁷J. Wang, A. Misra, and J. P. Hirth, *Phys. Rev. B* **83**(6), 064106 (2011).
- ³⁸L. L. Li, P. Zhang, Z. J. Zhang, and Z. F. Zhang, *Sci. Rep.* **4**, 3744 (2014).
- ³⁹D. Bufford, Y. Liu, J. Wang, H. Wang, and X. Zhang, *Nat. Commun.* **5**, 4864 (2014).
- ⁴⁰W. B. Jiang, Q. P. Kong, P. Cui, Q. F. Fang, D. A. Molodov, and G. Gottstein, *Phil. Mag.* **90**(6), 753(2010).
- ⁴¹V. Randle, *Acta Mater.* **52**(14), 4067 (2004).
- ⁴²V. Randle and G. Owen, *Acta Mater.* **54**(7), 1777 (2006).

Figure captions:

Fig. 1 (a) $\Sigma 3$ boundaries in DPD-ed sample with $\varepsilon=1.31$; (b) $\langle 111 \rangle$ and $\langle 101 \rangle$ pole figures for Grains 1 and 2 in Fig. 1(a); and (c) the points of trace vectors of fifty-six $\Sigma 3$ boundaries on the (001) stereographic projection comparing with the great circles of $\{112\}$ plane.

Fig. 2 (a) Two-layer EBSD result for DPD-ed sample with $\varepsilon=0.84$; and (b and c) EBSD maps for Layer 1 and 2, respectively.

Fig. 3 (a) Fraction of each type of CSL boundaries in total CSL boundaries at different strains (the type of CSL boundaries on horizontal axis varies from $\Sigma 3$ to $\Sigma 49c$, of which the detail can be found in TSL OIM software for EBSD analysis); and (b) fraction of CSL boundaries in high-angle boundaries ($\theta > 15^\circ$) at different strains.

Fig. 4 (a and b) EBSD images showing coexistence of different types of CSL boundaries in the samples with $\varepsilon=0.27$ and 0.84 , respectively; (c) misorientation profiles measured along Line 1 in Fig. 4(a); and (d) the points of trace vectors of low-angle ($< 15^\circ$) DB boundaries on the (001) stereographic projection comparing with the great circles of $\{111\}$ planes.

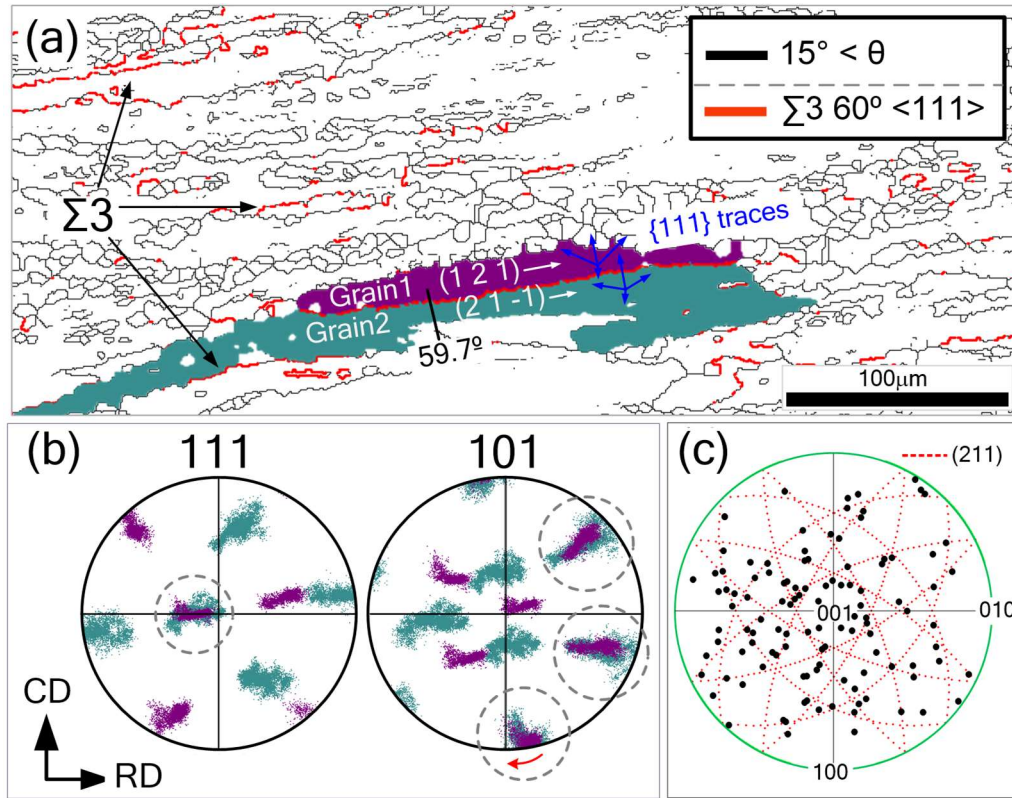


Fig. 1 (a) $\Sigma 3$ boundaries in DPD-ed sample with $\varepsilon=1.31$; (b) $\langle 111 \rangle$ and $\langle 101 \rangle$ pole figures for Grains 1 and 2 in Fig. 1(a); and (c) the points of trace vectors of fifty-six $\Sigma 3$ boundaries on the (001) stereographic projection comparing with the great circles of $\{112\}$ plane. (CD: compression direction; RD: radial direction; all the EBSD maps and pole figures in the present paper are with a same arrangement of directions)

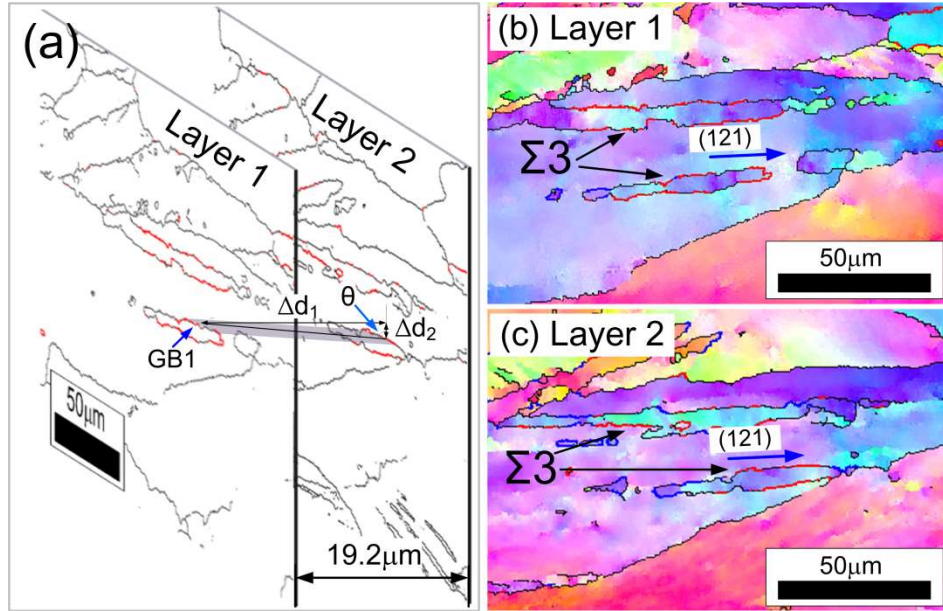


Fig. 2 (a) Two-layer EBSD result for DPD-ed sample with $\epsilon=0.84$; and (b and c) EBSD maps for Layer 1 and 2, respectively.

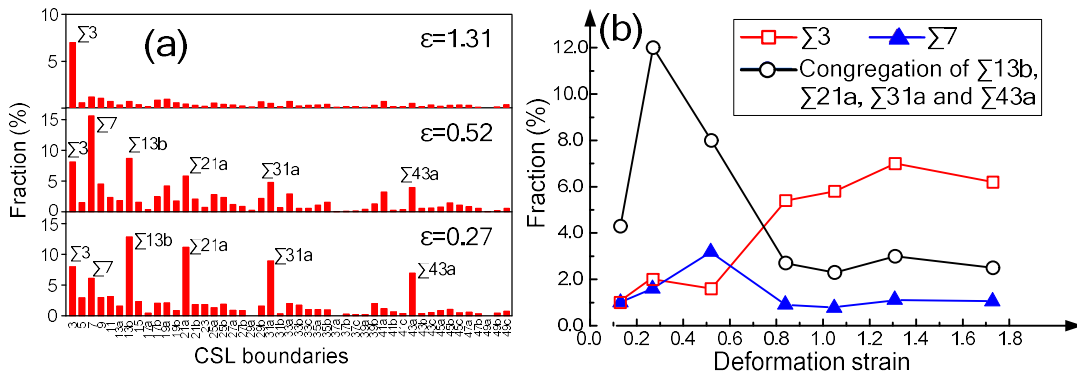


Fig. 3 (a) Fraction of each type of CSL boundaries in total CSL boundaries at different strains (the type of

CSL boundaries on horizontal axis varies from $\Sigma 3$ to $\Sigma 49c$, of which the detail can be found in TSL OIM software for EBSD analysis); and (b) fraction of CSL boundaries in high-angle boundaries ($\theta > 15^\circ$) at different strains.

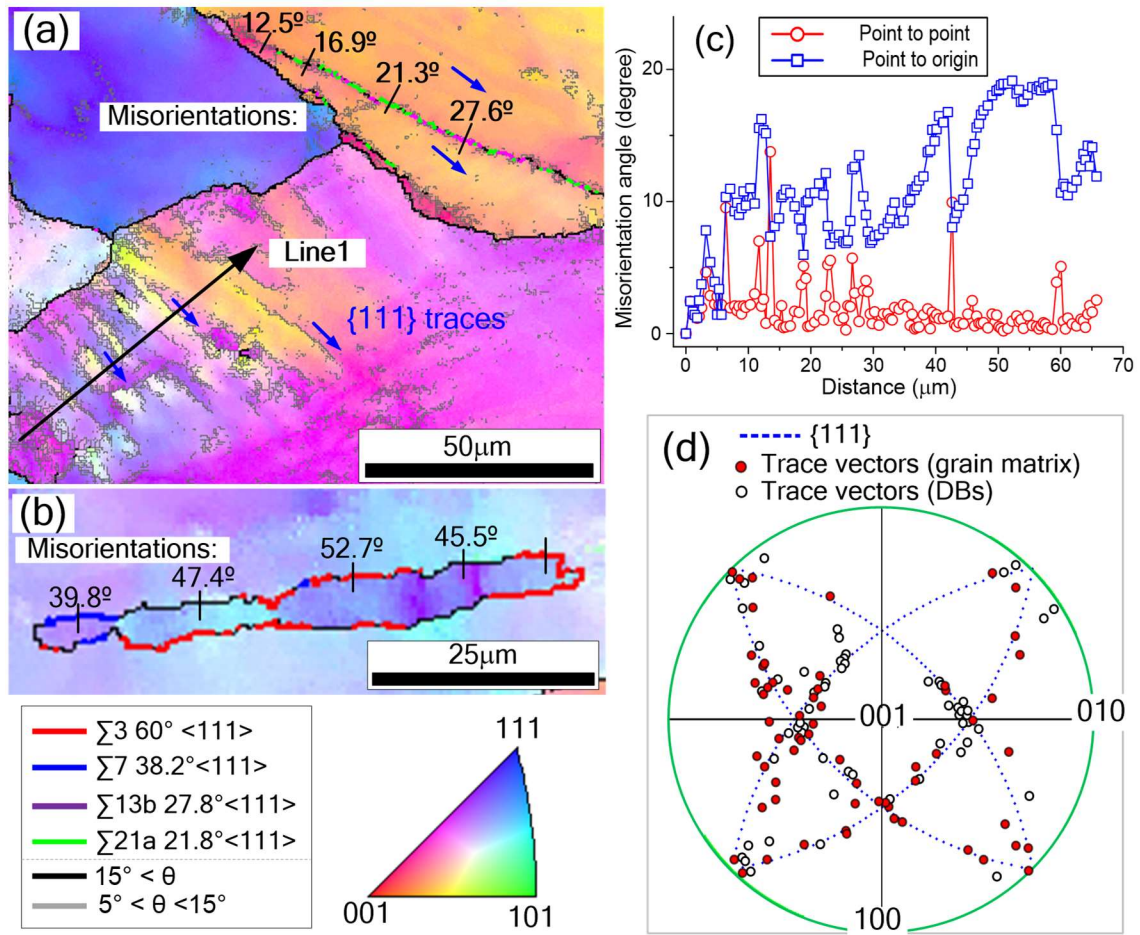


Fig. 4 (a and b) EBSD images showing coexistence of different types of CSL boundaries in the samples with

$\varepsilon=0.27$ and 0.84 , respectively; (c) misorientation profiles measured along Line 1 in Fig. 4(a); and (d) the points of trace vectors of low-angle ($<15^\circ$) DB boundaries on the (001) stereographic projection comparing with the great circles of $\{111\}$ planes.